Revealing the intrinsic electronic structure and complex fermiology of YRu_2Si_2 using angle-resolved photoemission spectroscopy

Anup Pradhan Sakhya,[1] Sabin Regmi,[1] Milo Sprague,[1] Mazharul Islam Mondal,[1] Iftakhar Bin Elius,[1] Nathan Valadez,[1] Andrzej Ptok,[2] Dariusz Kaczorowski,[3] and Madhab Neupane[1,*]

[1]*Department of Physics, University of Central Florida, Orlando, Florida 32816, USA*

[2]*Institute of Nuclear Physics, Polish Academy of Sciences, W. E. Radzikowskiego 152, PL-31342 Kraków, Poland*

[3]*Institute of Low Temperature and Structure Research, Polish Academy of Sciences, ulica Okólna 2, 50-422 Wrocław, Poland*

(Received 15 November 2023; revised 16 July 2024; accepted 16 August 2024; published 3 September 2024)

We performed a detailed study of the intrinsic electronic structure of YRu_2Si_2 employing angle-resolved photoemission spectroscopy (ARPES) and density-functional theory (DFT) based first-principles calculations. Electrical and magnetic measurements were conducted on well-oriented high-quality single crystals. Bulk physical measurements indicate that the compound exhibits slightly enhanced Pauli paramagnetic behavior, accompanied by electrical transport properties reminiscent of metals. Our ARPES data reveal fourfold symmetric Fermi surface with weakly dispersing bands around the $\overline{\mathrm{N}}$ point originating from Ru d orbitals. We observed the anisotropic characteristics of the band near the $\overline{\mathrm{N}}$ point, showing weak dispersion in the $\overline{\mathrm{X}}$-$\overline{\mathrm{N}}$-$\overline{\mathrm{X}}$ direction and minimal dispersion along the $\overline{\mathrm{N}}$-$\overline{\Gamma}$-$\overline{\mathrm{N}}$ direction. The electronic band structure near the Fermi level is primarily governed by the Ru d orbital, with minor contributions from the Y d and Si p orbitals. Polarization-dependent ARPES results indicate the multiband and multiorbital band character of YRu_2Si_2. Due to the negligible correlation effect, the observed ARPES data are found to be in good agreement with the DFT results.

DOI: 10.1103/PhysRevB.110.125104

I. INTRODUCTION

A wide range of physical properties are displayed by compounds with AB_2X_2 stoichiometry and $ThCr_2Si_2$-type crystal structure. Their peculiar physical properties arise from the alternating stacks of quasi-two-dimensional A and B_2X_2 layers in this series of compounds [1,2]. There are numerous elemental combinations for which the $ThCr_2Si_2$ derivatives exist. Alkali, alkaline earth, rare earth, or actinoid metals can make up the A cations, while the entire family of transition metals may occupy the B sites. The third, fourth, and fifth main group elements can occupy the X sites [3]. The valence electron count and, consequently, the magnetic ground states can vary due to the flexibility in the site occupancies. Iron-based superconductors with over 450 distinct compounds [4] and heavy fermions, such as $YbRh_2Si_2$ [5], $CeCu_2Si_2$ [6], and $CeRu_2Si_2$ [7], also possess the same crystal structure. In the context of heavy fermion systems, particularly, the phases containing cerium and uranium have received a great deal of attention during the past 30 years [3]. $CeRu_2Si_2$ is a well-known nonmagnetic Kondo lattice compound with a high electronic specific heat coefficient of 350 mJ/K^2 mol [8]. The f electron in $CeRu_2Si_2$ was found to exhibit itinerant behavior [9]. The electronic structure and Fermi surfaces of $LaRu_2Si_2$ have been thoroughly investigated through band structure calculations [10], de Haas–van Alphen (dHvA) effect measurements [11,12], and angle-resolved photoemission spectroscopy (ARPES) measurements [13]. At extremely low temperatures, superconductivity is demonstrated in several AB_2X_2 phases such as YPt_2Si_2 [14], YIr_2Si_2 [15], YRh_2Si_2, and YPd_2Si_2 [16]. Recently, the discovery of a square magnetic-skyrmion lattice in $GdRu_2Si_2$ which also crystallizes in the $ThCr_2Si_2$ structure with $I4/mmm$ space symmetry [9,17,18], has further generated enormous research interest because it hosts the shortest-period skyrmion lattice ever discovered and it does not possess a geometrically frustrated lattice [19]. This is important because it may have applications in quantum computing and memory devices [20]. Furthermore, recent research has uncovered the presence of flat bands located at the X points of the Brillouin zone (BZ) in the unconventional superconductor YFe_2Ge_2, which has the same $ThCr_2Si_2$-type crystal structure. These flat bands primarily consist of d_{xz} and d_{yz} orbitals [21]. YRu_2Si_2 is another compound possessing the same crystal structure as $CeRu_2Si_2$ but lacks any $4f$ states. While studies on the magnetoresistance and the dHvA effect of YRu_2Si_2 have been reported [11,12], the material remains relatively unexplored despite the growing interest in compounds with $ThCr_2Si_2$-type crystal structures.

In this paper, we report the electronic structure of YRu_2Si_2 determined by combining ARPES and density-functional theory (DFT) calculations. Bulk physical measurements reveal that the compound is a slightly enhanced Pauli paramagnet with metalliclike electrical transport properties. Our ARPES measurements indicate multiple pockets at the Fermi level E_F, which is consistent with the metallic nature of this sample. We notice a flattened region of the spectra along the $\overline{\mathrm{N}}$-$\overline{\Gamma}$-$\overline{\mathrm{N}}$ direction which exhibits weak dispersion along the $\overline{\mathrm{X}}$-$\overline{\mathrm{N}}$-$\overline{\mathrm{X}}$ direction. This indicates the anisotropic nature of this band,

*Contact author: madhab.neupane@ucf.edu

 ©2024 American Physical Society

which originates from Ru *d* orbitals. We also observe a Dirac-like electron pocket at the $\overline{X}$ point.

II. METHODS

A. Single-crystal growth and characterization

Single crystals of YRu_2Si_2 were grown using the Czochralski pulling technique in an ultrapure argon atmosphere using a tetra-arc furnace from GES Corp., Japan. Elemental constituents with high chemical purity (Y: 99.97 wt %, Ru: 99.95 wt %, Si: 99.9999 wt %) were taken in the stoichiometric ratio. The pulling rate was 10 mm/h, and the copper hearth's rotation speed was 3 rpm. The so-prepared ingot was wrapped with Ta foil, sealed in an evacuated silica tube, and annealed at 900 °C for 2 weeks. The product was checked for its crystal-chemical quality by utilizing energy-dispersive x-ray (EDX) analysis, performed using an FEI scanning electron microscope and equipped with an EDAX Genesis XM4 spectrometer. Powder x-ray diffraction (XRD) was carried out on a PANanalytical X'pert Pro diffractometer with Cu $K\alpha$ radiation. The results of these XRD and EDX experiments are presented in Figs. S1 and S2, respectively, in the Supplemental Material (SM) [22]. Single-crystalline specimens used in the physical properties measurements were oriented by means of single-crystal Laue x-ray backscattering, implemented in a Proto LAUE-COS system.

B. Transport measurements

Electrical resistivity measurements were performed in the temperature interval 2–300 K using a Quantum Design PPMS-9 platform. The electrical leads were made of 50 μm silver wires attached to a bar-shaped specimen with silver-epoxy paste. The experiment was performed employing a standard four-point AC technique with the electric current flowing within the tetragonal plane of the YRu_2Si_2 crystal. The resistivity measured at room temperature was about 32 μΩ cm, and that at 2 K was equal to 0.4 μΩ cm. The large ratio between these two values (residual resistivity ratio = 80) proves the high quality of the sample investigated.

C. ARPES measurements

ARPES measurements were performed at the Stanford Synchrotron Radiation Lightsource (SSRL), endstation 5-2. Measurements were carried out at a temperature of 15 K. The pressure in the UHV range was maintained at better than 1×10^{-10} Torr. The angular and energy resolutions were set to be better than 0.2° and 15 meV, respectively. Measurements were performed using photon energies in the range of 30–90 eV with both linear horizonal (LH) and linear vertical (LV) polarizations.

D. *Ab initio* calculations

DFT calculations were performed using the projector augmented-wave potentials [23] implemented in the Vienna Ab initio Simulation Package (VASP) [24–26]. Calculations were made within the generalized gradient approximation in the Perdew, Burke, and Ernzerhof parametrization [27]. The energy cutoff of the plane-wave expansion was set to 400 eV. In the calculation, we used the experimental lattice vectors as well as atomic positions [3]. The theoretically obtained Fermi level is overestimated with respect to the experimentally observed Fermi level by around 0.2 eV. In our study, we present the theoretical results with the shifted Fermi level. The electronic band structure was also evaluated within QUANTUM ESPRESSO [28–30] with PSLIBRARY [31]. The exact results of the electronic band structure calculation, performed for the primitive unit cell, were used to find the tight-binding model in the basis of the maximally localized Wannier orbitals [32–34]. This calculation was performed using the WANNIER90 software [35–37]. In our calculations, we used the $8 \times 8 \times 8$ full $\boldsymbol{k}$-point mesh, starting from the *p* orbitals of Si, as well as the *d* and *s* orbitals for Y and Ru. Finally, the 24-orbital tight-binding model of YRu_2Si_2 was used to investigate the surface Green's function for the semi-infinite system [38], using the WANNIERTOOLS [39] software.

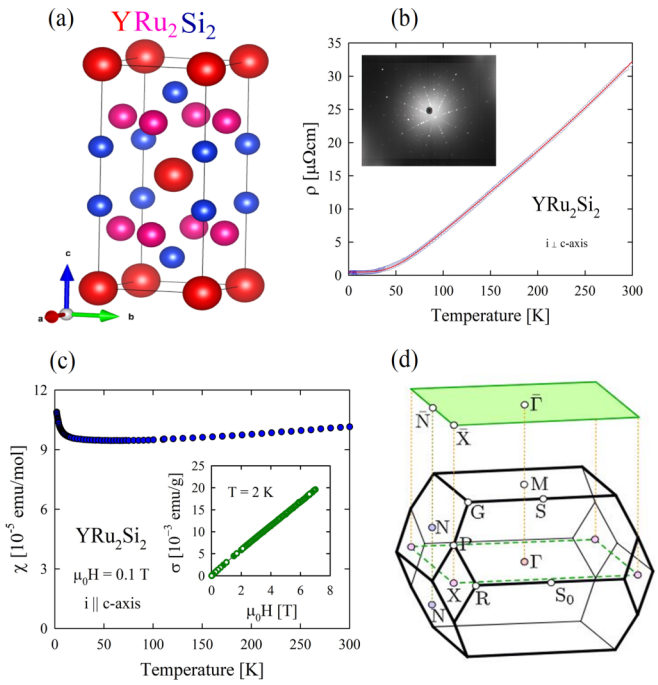

FIG. 1. Crystal structure and sample characterization of YRu_2Si_2. (a) Crystal structure of YRu_2Si_2, where the red, pink, and blue solid spheres denote the Y, Ru, and Si atoms, respectively. (b) Temperature dependence of the electrical resistivity measured with electric current flowing in the tetragonal plane. The solid line represents the BGM fit discussed in the text. The inset shows the Laue diffraction pattern taken from the (001) plane. (c) Temperature dependence of the magnetic susceptibility measured in a magnetic field of 0.1 T applied along the tetragonal axis. The inset displays the magnetization isotherm measured at 2 K with increasing (solid symbols) and decreasing (open symbols) field applied along the tetragonal axis. (d) Bulk Brillouin zone (BZ) and its projection onto the (001) surface BZ. High-symmetry points are marked.

III. RESULTS AND DISCUSSION

A. Crystal structure

The crystal structure of YRu_2Si_2 is shown in Fig. 1(a). The compound crystallizes in the $ThCr_2Si_2$-type body-centered tetragonal structure ($I4/mmm$, space group 139), with lattice

constants $a = b = 4.1580(6)$ Å and $c = 9.546(2)$ Å [3]. The primitive unit cell contains one Y atom at the $2a$ (0,0,0) Wyckoff position, two Ru atoms at the $4d$ (0,1/2,1/4) Wyckoff position, and two Si atoms at the $4e$ (0,0,0.3684) Wyckoff position [3]. The crystal structure of this material is mainly formed by edge-sharing $RuSi_4$ tetrahedra layers in the *ab* plane, which are separated by Y atoms. An exemplary Laue diffractogram is shown in the inset in Fig. 1(b). A clear tetragonal symmetry pattern with well-defined sharp spots proves the high crystalline quality of the sample investigated, and a comparison of the experimental data with the simulated diffractogram indicates its (001) orientation.

B. Main transport properties

The temperature variation of the resistivity $\rho(T)$, presented in Fig. 1(b), is typical for metals. The experimental $\rho(T)$ data can be well described by the Bloch-Grüneissen-Mott (BGM) formula [40]:

$$\rho(T) = \rho_0 + 4RT\left(\frac{T}{\Theta_D}\right)^4 \int_0^{\Theta_D/T} \times \frac{x^5 dx}{(e^x - 1)(1 - e^{-x})} - KT^3, \quad (1)$$

where ρ_0 stands for the residual resistivity due to static defects in the crystal lattice, the second term describes the phonon contribution to the total resistivity, and the third one represents *s*-*d* interband scattering processes. The solid line in Fig. 1(b) is a least-squares fit of the experimental $\rho(T)$ curve to the above expression, yielding the BGM parameters: $\rho_0 = 0.4(1)$ μΩ cm, the Debye temperature $\Theta_D = 306(4)$ K, $R = 0.09(7)$ μΩ cm/K and $K = 1.7 \times 10^{-7}$ μΩ cm/K^3. It is worth noting that the small value of the latter parameter, directly related to the small curvature of $\rho(T)$ at high temperatures, implies that the scattering of conduction electrons via Mott-type processes in YRu_2Si_2 is almost negligible. Magnetic measurements were performed in the temperature range from 2 to 300 K and in magnetic fields up to 7 T using a Quantum Design MPMS-XL superconducting quantum interference device magnetometer. Figure 1(c) presents the temperature dependence of the molar magnetic susceptibility $\chi(T) = M/H$ measured in a magnetic field of 0.1 T applied along the crystallographic c axis of the tetragonal unit cell of YRu_2Si_2. The compound exhibits an almost temperature-independent $\chi(T)$ of the order of 10^{-4} emu/mol, implying its weakly enhanced Pauli paramagnetic character. In line with this finding, the magnetization isotherm $\sigma(H)$ taken at 2 K shows a straight-line and fully reversible behavior up to the highest measured magnetic field of 7 T, where σ reaches a small value [see the inset in Fig. 1(c)]. In Fig. 1(d), the bulk BZ and its projection on the (001) surface are shown, and various high-symmetry points are labeled.

C. Theoretical band structure

The Fermi surface (FS) of YRu_2Si_2 is presented in Fig. 2. The obtained FS can be directly compared with that obtained earlier for other 122 compounds. In practice, the obtained FS has qualitatively the same shape as that reported for $ThRu_2Si_2$ [2,41]. The difference in the observed Fermi pocket sizes arises from variations in the band structure complexity and

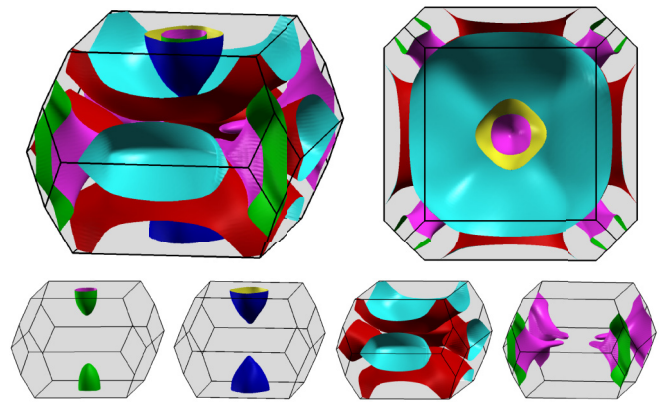

FIG. 2. The Fermi surface (FS) of YRu_2Si_2 with $I4/mmm$ symmetry. Top panels present the "full" FS, while bottom panels present separate pockets.

the position of the Fermi level. In the case of YRu_2Si_2, the Fermi level is lower with respect to that reported in $ThRu_2Si_2$. Such a Fermi level shift can also be a consequence of different lattice constants, stronger correlation within f orbitals, or d-f hybridization. Nevertheless, the FS of XRu_2Si_2 compounds with f electrons strongly depend on the electronic configuration [13], and the similarity to $ThRu_2Si_2$ may be incidental. In fact, the FSs of other XRu_2Si_2 compounds with f electrons present many more differences [13]. Similarly, the Eu-based 122 system shows Dirac electronic states [42,43].

The shape of the FS pockets exhibits a three-dimensional (3D) character of the electrons. This property is in contradiction to other 122 compounds with relatively large c/a ratios. For example, in the case of KFe_2As_2 with $c/a \approx 3.6$, the FS takes the form of cylinders [44–47], revealing a two-dimensional nature of the electrons. This is a consequence of the weak coupling between FeAs layers. Nonetheless, for the collapsed tetragonal phase (under pressure), c/a can decrease to 2.7. In this situation, the coupling between layers increases, leading to a change in the FS topology [46,47]. As a result, electrons acquire a 3D character (dispersion along z), while the FS is very similar to that presented in Fig. 2. Moreover, such features of the FS is characteristic of the 122 compounds with relatively small c/a, like YFe_2Ge_2 [48]. The small c/a ratio, as well as the 3D character of the FS, indicates strong coupling between Ru-Si layers.

The theoretically obtained electronic band structure and density of states are presented in Fig. 3. The electronic band structure possesses a relatively complex structure around the Fermi level [Fig. 3(a)]. The splitting of the bands introduced by spin-orbit coupling is weak, indicating a negligible role of spin-orbit coupling in the compound [see the orange and blue lines in Fig. 3(a) comparing the band structures obtained without and with spin-orbit coupling]. In practice, only a small splitting of the bands along the Γ-S path is visible. The electronic density of states presented in Fig. 3(b) clearly shows the dominant role of the Ru d orbitals. A small contribution from the Si p and Y d orbitals around the Fermi level is also observed. The Si s states are located deep below the Fermi level, around −9 eV, and do not play any significant role. Such contributions are further supported by the electronic

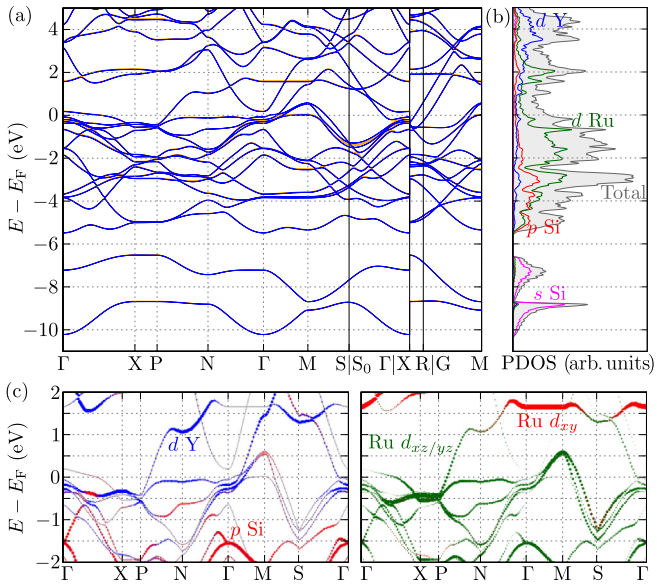

FIG. 3. (a) Theoretically obtained electronic bulk band structure and (b) the corresponding density of states. The electronic band structure calculated in the absence and presence of spin-orbit coupling is represented by orange and blue lines, respectively. (c) The orbital projection of the band structure in close vicinity to the Fermi level.

band structure projected onto the atomic orbitals [Fig. 3(c)]. In close vicinity to the Fermi level, the Ru $d_{xz/yz}$ orbitals play a dominant role, with a small contribution from the Si p and Y d orbitals.

We can expect that the electronic band structure of YRu_2Si_2 will be similar to that of other XRu_2Si_2 compounds. For instance, $LaRu_2Si_2$ is an isostructural compound that also lacks f electrons and has similar lattice constants ($a = b =$ 4.19 Å and $c = 9.80$ Å) [49]. What is surprising is that the band structure of $LaRu_2Si_2$ possesses significant differences compared to YRu_2Si_2. For example, we observe nearly flat bands along the P-N-Γ path (see Fig. 3), while in $LaRu_2Si_2$, several holelike bands with clearly parabolic shapes are observed. The situation becomes more complex in the case of XRu_2Si_2 compounds with f electrons. In such cases, the band structures differ significantly among the family members due to the f states located around the Fermi level [13].

D. The ARPES measurements

Next, we perform ARPES measurements to reveal the electronic structure of YRu_2Si_2. Figure 4(a) shows the FS and constant-energy contours (CECs) at various binding energies using a photon energy of 68 eV. Experimental FS maps and CECs are presented in Fig. 4(a), and the DFT-calculated FS and CECs are presented in Fig. 4(b). Both experimental and theoretical FSs are provided with BZs marked with high-symmetry points. Multiple pockets are observed at the FS, which indicates the complex fermiology of this material. We observe multiple circular-shaped pockets at the $\overline{\Gamma}$ point, an ellipsoidal pocket at the $\overline{N}$ point, and a pocket at the $\overline{X}$ point. The energy contours presented in the right hand side of Figs. 4(a) and 4(b) delineate how the band dispersions evolve with binding energies. The energy pockets at the $\overline{\Gamma}$ and $\overline{N}$ points grow bigger in size with the increase in binding energy, indicating the holelike nature of the bands, whereas the pocket at the $\overline{X}$ point decreases in size, indicating the electronlike nature. Several bulk pockets appear at higher binding energies, which can be clearly visualized from the CEC plots at binding energies of 200, 300, and 400 meV. The experimental FS and the CECs of the material are quite well reproduced from the

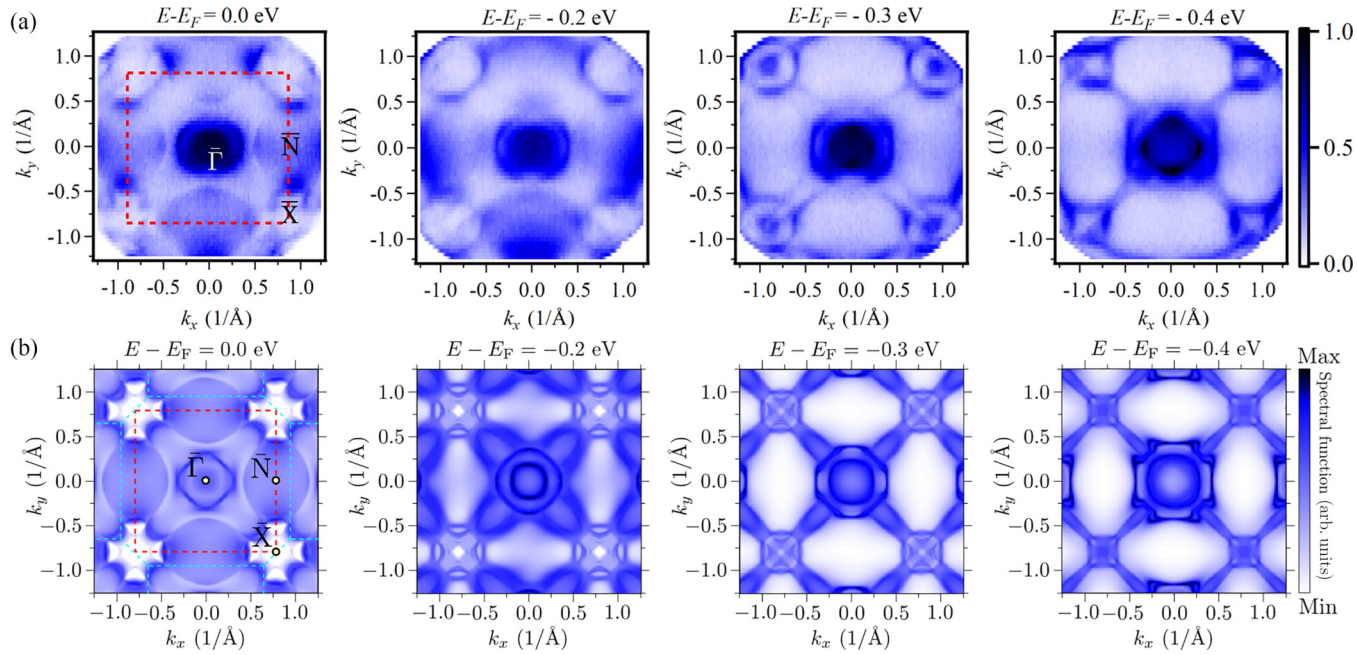

FIG. 4. FS and constant-energy contours. (a) ARPES-measured FS (first panel) and constant energy contours measured using a photon energy of 68 eV at various binding energies as indicated above each plot. (b) Respective FS and constant-energy contours obtained from DFT calculations.

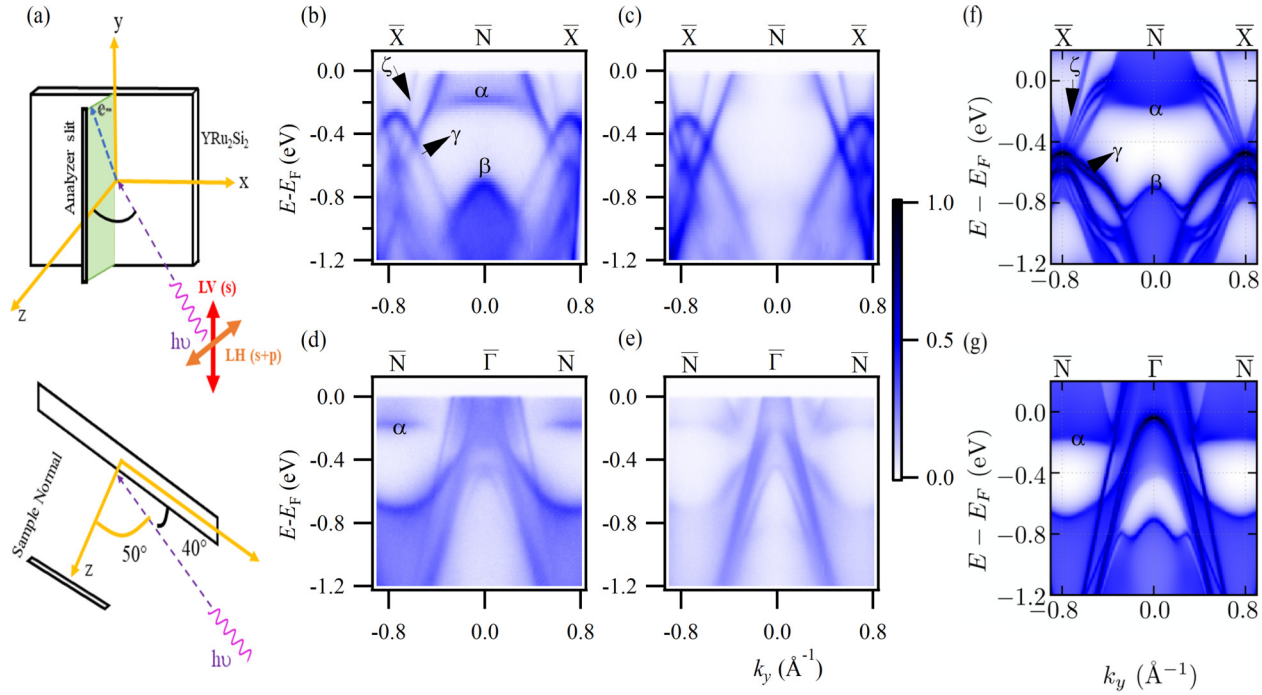

FIG. 5. Polarization-dependent ARPES spectra of YRu_2Si_2. (a) Schematic of the experimental geometry used in the ARPES experiments. Experimental band dispersion along the $\overline{X}$-$\overline{N}$-$\overline{X}$ direction using (b) LH polarization and (c) LV polarization. Experimental band dispersion along the $\overline{N}$-$\overline{\Gamma}$-$\overline{N}$ direction using (d) LH polarization and (e) LV polarization. DFT-calculated band structure along (f) the $\overline{X}$-$\overline{N}$-$\overline{X}$ direction and (g) $\overline{N}$-$\overline{\Gamma}$-$\overline{N}$ direction.

DFT calculations, as shown in Fig. 4(b). The exception of some pockets such as the rhombus pocket at the $\overline{\Gamma}$ point can be explained by the polarization dependence, which can be seen from the polarization-dependent FS maps presented in Figs. S3 and S4 in the SM [22].

While there have not been any electronic structure investigations utilizing DFT or ARPES for YRu_2Si_2, dHvA measurements have been reported [11,12]. In contrast, $LaRu_2Si_2$, which has a similar crystal structure, as discussed previously, has undergone extensive examination via both dHvA and ARPES [10–13]. Therefore, we compare our ARPES findings with both dHvA for $LaRu_2Si_2$ and YRu_2Si_2 and ARPES for $LaRu_2Si_2$ in the following. The FS of YRu_2Si_2, as observed, shows significant congruence with the dHvA measurements [11,12] and ARPES measurements [13], especially in relation to the pocket at the $\overline{N}$ point. A large, distinct closed-hole FS with an ellipsoidal shape at the Z point, corresponding to the

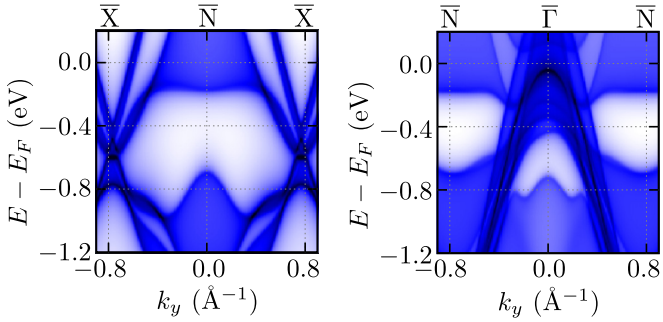

FIG. 6. Theoretical results of the spectrum along the $\overline{X}$-$\overline{N}$-$\overline{X}$ and $\overline{N}$-$\overline{\Gamma}$-$\overline{N}$ directions coming from only bulk states.

$\overline{N}$ point in our ARPES data, was observed in both $LaRu_2Si_2$ and YRu_2Si_2 from both dHvA and ARPES measurements [10–13]. Additionally, three hole pockets were observed at the Z point for $LaRu_2Si_2$ from both dHvA and ARPES measurements, whereas one hole pocket was observed for YRu_2Si_2 [10–13]. Upon comparison, we confirm a large ellipsoidal hole pocket centered at the $\overline{N}$ point, which aligns well with the reported dHvA and ARPES measurements. However, discrepancies arise because additional hole pockets at the $\overline{N}$ point, resembling a rugby ball shape, were not detected in our ARPES data. Additionally, our ARPES data reveal multiple holelike pockets at the $\overline{\Gamma}$ point, particularly emphasized in LH polarized data compared to LV polarized data (see Fig. 5), which were not observed in dHvA measurements and ARPES measurements [10–13].

To examine the details of the band structure, we present the ARPES-measured band dispersion along the $\overline{X}$-$\overline{N}$-$\overline{X}$ and $\overline{N}$-$\overline{\Gamma}$-$\overline{N}$ directions in Fig. 5. We performed polarization-dependent ARPES measurements to investigate the potential multiorbital characteristics of YRu_2Si_2. The experimental geometry of the polarization-dependent ARPES is presented in Fig. 5(a). ARPES provides a unique opportunity to directly examine the orbital texture of K states with different symmetries by using photon polarization selection rules [50]. The intensity I measured in ARPES experiments is strongly dependent on the transition matrix elements of the photoemission process and can be expressed as $I \propto \langle \Psi_f | \vec{A} \cdot \vec{p} | \Psi_i \rangle$, where $\vec{A}$ is the electromagnetic gauge and $\vec{p}$ is the electron momentum. $\vec{A}$ exhibits the same spatial mirror symmetry as the electric field $\vec{E}$ of the incident polarized photon beam, while $|\Psi_i\rangle$ and $|\Psi_f\rangle$ represent the electron wave function in

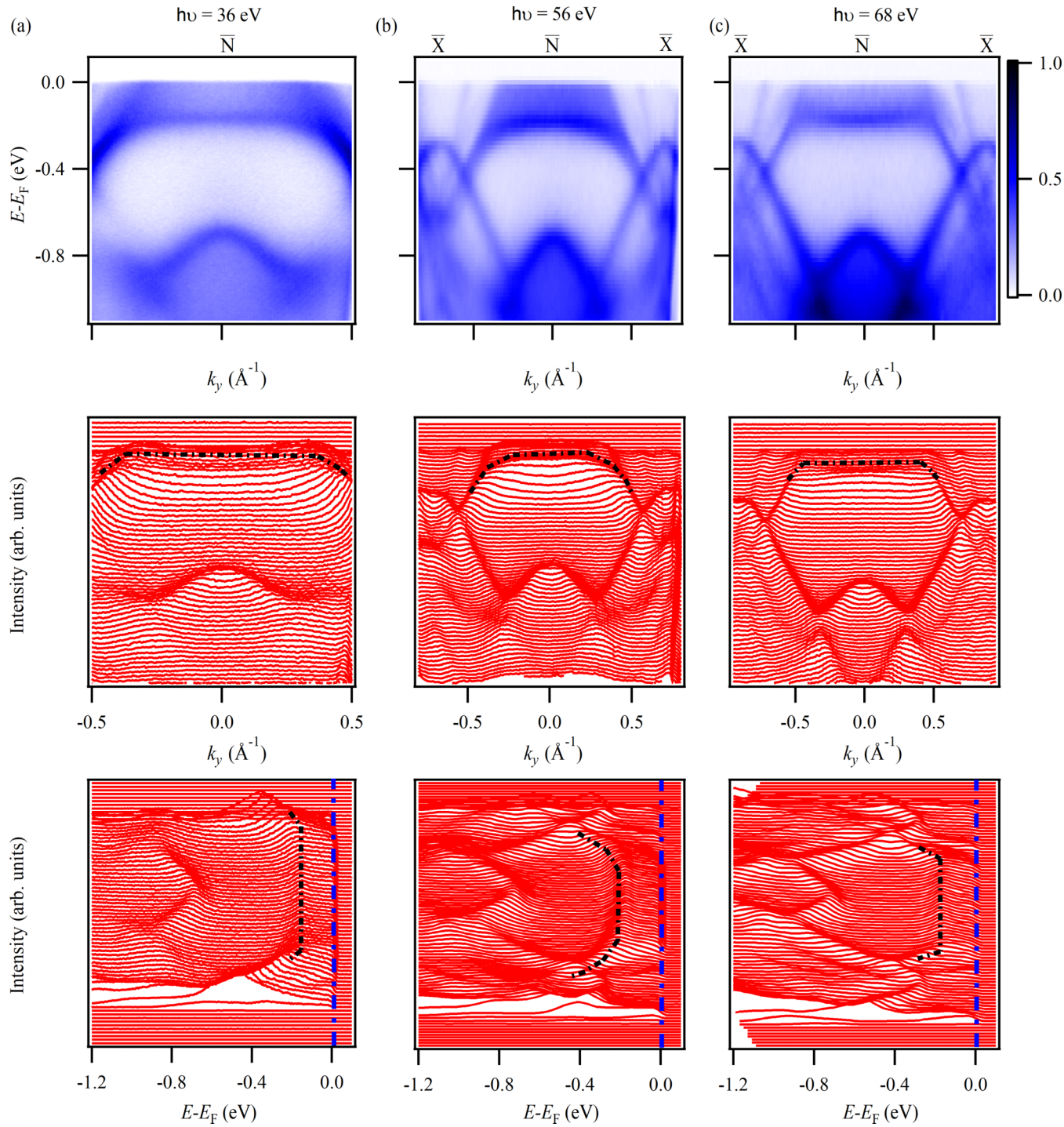

FIG. 7. Photon-energy-dependent band dispersion along the $\overline{\mathrm{X}}$-$\overline{\mathrm{N}}$-$\overline{\mathrm{X}}$ direction. Experimentally measured band dispersion along the $\overline{\mathrm{X}}$-$\overline{\mathrm{N}}$-$\overline{\mathrm{X}}$ direction using photon energies of (a) 36 eV, (b) 56 eV, and (c) 68 eV. The middle and bottom panels are the momentum distribution curves (MDCs) and the energy distribution curves (EDCs) for the respective plots in (a)–(c). The black dashed lines overlaid in the MDC and EDC plots are the hand-drawn curves showing the weak dispersion of the flat bands for clarity, and the blue dashed lines in EDCs represent the Fermi level.

the solid (initial state) and the wave function of the excited photoelectron (final state), respectively [51,52]. The incident beam and the normal to the sample surface together form a mirror plane. Given that the final state $|\Psi_f\rangle$ of photoelectrons can be approximated by a plane wave with its wave vector in the mirror plane, it is always even in relation to the mirror plane [51,52].

The measurements were performed for a photon energy of 62 eV using both LH and LV polarizations. We observe multiple bands crossing E_F. The electronlike pocket at the

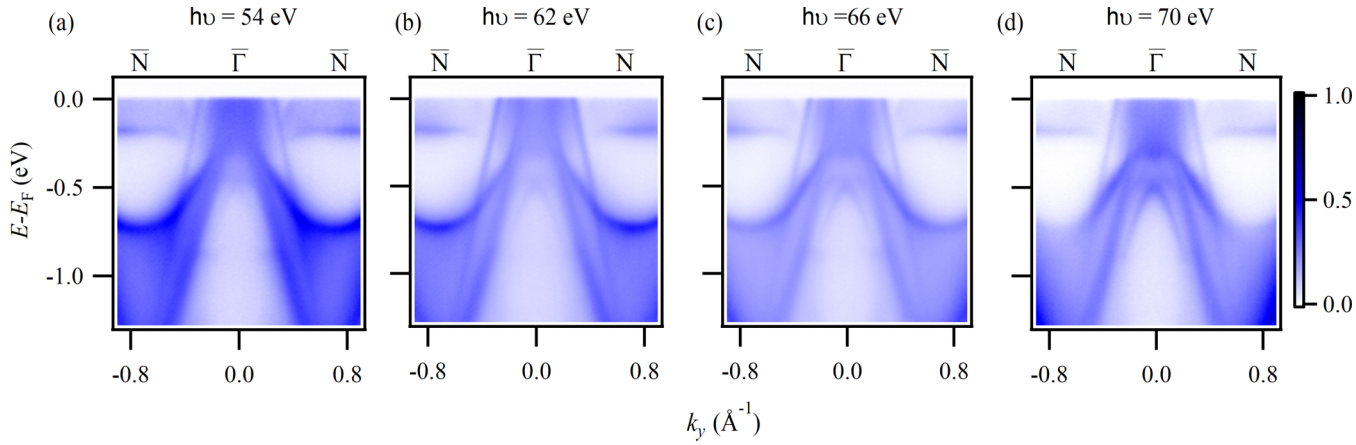

FIG. 8. Photon-energy-dependent band dispersion along the $\overline{\mathrm{N}}$-$\overline{\Gamma}$-$\overline{\mathrm{N}}$ direction. (a)–(d) Experimentally measured band dispersion along the $\overline{\mathrm{N}}$-$\overline{\Gamma}$-$\overline{\mathrm{N}}$ direction for various photon energies as indicated above the plots using LH polarization.

$\overline{\mathrm{X}}$ point as discussed above interestingly reveals a Dirac-like band (denoted ζ) which is marked by black arrow in Fig. 5(b). This Dirac-like state seems to be quite intense in both LH and LV polarization measurements, as can be seen in Figs. 5(b) and 5(c) (see also Fig. S5 in the SM [22]). We also observe a flattened region of the spectra around the $\overline{\mathrm{N}}$ point (denoted α) which is found to be very sensitive to polarization measurement because this band is intense when measured with LH polarization and strongly suppressed when measured with LV polarization [see Figs. 5(b)–5(e)]. Another holelike band around 800 meV below the E_F (denoted β) is found to be very sensitive to polarization measurements as the intensity of this band is strong in LH polarization; however, it is almost absent in LV polarization [see Figs. 5(b) and 5(c)].

In the LH (LV) geometry $\vec{A} \cdot \vec{p}$ is odd (even) with respect to the mirror plane. Hence, taking into account the spatial symmetry of the Ru $3d$ orbitals, when the analyzer slit aligns with the high-symmetry directions as presented in Fig. 5, the photoemission intensity of specific even (odd) components of a band can be detected only with LH (or LV) polarized light. For instance, with respect to the yz mirror plane, LV excites even orbitals ($d_{x^2-y^2}$, d_{z^2}, and d_{yz}) and suppresses odd orbitals (d_{xy}, d_{xz}), respectively. Based on these selection rules and the orbital character of the bands obtained from DFT calculations [see Fig. 3(c)], the flattened region of the spectra around the $\overline{\mathrm{N}}$ high-symmetry point (denoted by α) is strongly dominated by Ru d_{xz} orbitals. Additionally, the band β originates from Ru d_{xz} orbitals. The DFT-calculated surface and bulk spectrum is presented in Figs. 5(f) and 5(g) and is in good agreement with the observed ARPES results where the flattened region of the spectra around the $\overline{\mathrm{N}}$ point and the Dirac-like band can be seen clearly. The above qualitative arguments obtained from polarization-dependent ARPES results, consistent with our DFT calculations, allow us to delineate the contribution from different orbitals to the electronic band structure of this material. We present the DFT-calculated bulk spectrum along the $\overline{\mathrm{X}}$-$\overline{\mathrm{N}}$-$\overline{\mathrm{X}}$ and $\overline{\mathrm{N}}$-$\overline{\Gamma}$-$\overline{\mathrm{N}}$ directions, including only the bulk states, in Fig. 6. By comparing Fig. 6 with Figs. 5(f) and 5(g), we observe that the γ band is not a bulk band but originates from surface states.

To further examine the dimensionality of these bands, we perform photon-energy-dependent ARPES measurements along the $\overline{\mathrm{X}}$-$\overline{\mathrm{N}}$-$\overline{\mathrm{X}}$ direction using photon energies of 36, 56, and 68 eV using LH polarization, as shown in Fig. 7. The flattened region of the spectra around the $\overline{\mathrm{N}}$ point seems to weakly disperse with the change in photon energy. The momentum distribution curves (MDCs) and the energy distribution curves (EDCs) are presented in the middle and bottom panels of Figs. 7(a)–7(c), corresponding to their respective photon energies. The black dotted lines in both the MDCs and the EDCs clearly reveal the weak dispersion of the band around the $\overline{\mathrm{N}}$ high-symmetry point. In Fig. 8 we present the photon-energy-dependent bands along the $\overline{\mathrm{N}}$-$\overline{\Gamma}$-$\overline{\mathrm{N}}$ direction using LH polarization. The band observed at the $\overline{\mathrm{N}}$ point seems to show no dispersion even with the change in photon energy from 54 to 70 eV. This is in contrast to the weak dispersion along the $\overline{\mathrm{X}}$-$\overline{\mathrm{N}}$-$\overline{\mathrm{X}}$ direction indicating the anisotropic dispersion of this Ru d-dominated band around the $\overline{\mathrm{N}}$ point. The slight variation in intensity is possibly due to the photoemission matrix element effect.

IV. CONCLUSIONS

In summary, we synthesized high-quality single crystals of YRu_2Si_2 and characterized them using various bulk measurement techniques such as x-ray diffraction, Laue diffraction, magnetization, and resistivity measurements. YRu_2Si_2 crystallizes in the $ThCr_2Si_2$ family of materials, belonging to the space group $I4/mmm$. Electrical resistivity measurements indicated its metallic behavior, whereas magnetization measurements exhibited slightly enhanced Pauli paramagnetic behavior. We reproduced the experimentally obtained ARPES spectra within the DFT calculations. The excellent agreement between the experimental results and the theoretically obtained spectra indicates a weak role of the correlation effects, in contrast to the iron-based 122 compounds [53]. We found the anisotropic nature of the band around the $\overline{\mathrm{N}}$ point because it shows weak dispersion along the $\overline{\mathrm{X}}$-$\overline{\mathrm{N}}$-$\overline{\mathrm{X}}$ direction and negligible dispersion along the $\overline{\mathrm{N}}$-$\overline{\Gamma}$-$\overline{\mathrm{N}}$ direction. We also observed a Dirac-like state at the $\overline{\mathrm{X}}$ point, with a nearly linear crossing of the nontopological surface states. Additionally,

polarization-dependent ARPES results suggest the multiband and multiorbital nature of YRu_2Si_2. The electronic band structure around the Fermi level is dominated by Ru *d* orbitals, with a small contribution from Y *d* and Si *p* orbitals.

ACKNOWLEDGMENTS

M.N. acknowledges the support from the Air Force Office of Scientific Research MURI (Grant No. FA9550-20-1-0322) and National Science Foundation (NSF) CAREER Award No. DMR-1847962. A.P. acknowledges the support from the National Science Centre (NCN, Poland) under Project No. 2021/43/B/ST3/02166. The use of the Stanford Synchrotron Radiation Lightsource (SSRL) in the SLAC National Accelerator Laboratory is supported by the U.S. Department of Energy, Office of Science, Office of Basic Energy Sciences under Contract No. DE-AC02-76SF00515. We thank M. Hashimoto and D. Lu for the beamline assistance at SSRL endstation 5-2. Some figures in this work were rendered using the VESTA [54] and XCRYSDEN [55] software.

[1] R. Hoffmann, *Solids and Surfaces: A Chemist's View of Bonding in Extended Structures* (Wiley, Hoboken, NJ, 2021).
[2] S.-I. Fujimori, M. Kobata, Y. Takeda, T. Okane, Y. Saitoh, A. Fujimori, H. Yamagami, Y. Matsumoto, E. Yamamoto, N. Tateiwa, and Y. Haga, Phys. Rev. B **96**, 125117 (2017).
[3] C. Höting, H. Eckert, S. F. Matar, U. C. Rodewald, and R. Pöttgen, Z. Naturforsch. B **69**, 305 (2014).
[4] G. R. Stewart, Rev. Mod. Phys. **83**, 1589 (2011).
[5] O. Trovarelli, C. Geibel, S. Mederle, C. Langhammer, F. Grosche, P. Gegenwart, M. Lang, G. Sparn, and F. Steglich, Phys. Rev. Lett. **85**, 626 (2000).
[6] F. Steglich, J. Aarts, C. Bredl, W. Lieke, D. Meschede, W. Franz, and H. Schäfer, Phys. Rev. Lett. **43**, 1892 (1979).
[7] M. J. Besnus, J. P. Kappler, P. Lehmann, and A. Meyer, Solid State Commun. **55**, 779 (1985).
[8] D. Inoue, D. Kaido, Y. Yoshikawa, M. Minegishi, K. Matsumoto, S. Abe, and S. Murayama, Phys. Procedia **75**, 158 (2015).
[9] K. Hiebl, C. Horvath, P. Rogl, and M. J. Sienko, J. Magn. Magn. Mater. **37**, 287 (1983).
[10] H. Yamagami and A. Hasegawa, J. Phys. Soc. Jpn. **61**, 2388 (1992).
[11] R. Settai, H. Ikezawa, H. Toshima, M. Takashita, T. Ebihara, H. Sugawara, T. Kimura, K. Motoki, and Y. Ōnuki, Physica B (Amsterdam, Neth.) **206–207**, 23 (1995).
[12] H. Ikezawa, R. Settai, M. Takashita, N. Kimura, T. Ebihara, H. Sugawara, K. Motoki, Y. Ōnuki, T. Fukuhara, and K. Maezawa, J. Phys. Soc. Jpn. **64**, 3422 (1995).
[13] J. D. Denlinger, G. H. Gweon, J. W. Allen, C. G. Olson, M. B. Maple, J. L. Sarrao, P. E. Armstrong, Z. Fisk, and H. Yamagami, J. Electron Spectrosc. Relat. Phenom. **117–118**, 347 (2001).
[14] R. Shelton, H. Braun, and E. Musick, Solid State Commun. **52**, 797 (1984).
[15] M. Hirjak, P. Lejay, B. Chevalier, J. Etourneau, and P. Hagenmuller, J. Less-Common Met. **105**, 139 (1985).
[16] T. T. M. Palstra, G. Lu, A. A. Menovsky, G. J. Nieuwenhuys, P. H. Kes, and J. A. Mydosh, Phys. Rev. B **34**, 4566 (1986).
[17] M. Slaski and A. Szytula, J. Less-Common Met. **87**, L1 (1982).
[18] M. Ślaski, A. Szytuła, J. Leciejewicz, and A. Zygmunt, J. Magn. Magn. Mater. **46**, 114 (1984).
[19] N. D. Khanh, T. Nakajima, X. Yu, S. Gao, K. Shibata, M. Hirschberger, Y. Yamasaki, H. Sagayama, H. Nakao, and L. Peng, Nat. Nanotechnol. **15**, 444 (2020).
[20] S. Eremeev, D. Glazkova, G. Poelchen, A. Kraiker, K. Ali, A. Tarasov, S. Schulz, K. Kliemt, E. Chulkov, and V. Stolyarov, Nanoscale Adv. **5**, 6678 (2023).
[21] R. Kurleto, S. Acharya, C.-H. Wu, D. M. Narayan, B. S. Berggren, P. Hao, A. Shackelford, H. R. Whitelock, Z. Sierzega, M. Hashimoto, D. Lu, C. Jozwiak, R. P. Cline, D. Pashov, J. Chen, M. van Schilfgaarde, F. M. Grosche, and D. S. Dessau, arXiv:2311.09492.
[22] See Supplemental Material at http://link.aps.org/supplemental/10.1103/PhysRevB.110.125104 for powder x-ray diffraction data, energy-dispersive x-ray analysis, the polarization-dependent Fermi surface, and a zoomed-in view of the band dispersion around the $\overline{X}$ high-symmetry point.
[23] P. E. Blöchl, Phys. Rev. B **50**, 17953 (1994).
[24] G. Kresse and J. Hafner, Phys. Rev. B **49**, 14251 (1994).
[25] G. Kresse and J. Furthmüller, Phys. Rev. B **54**, 11169 (1996).
[26] G. Kresse and D. Joubert, Phys. Rev. B **59**, 1758 (1999).
[27] J. P. Perdew, K. Burke, and M. Ernzerhof, Phys. Rev. Lett. **77**, 3865 (1996).
[28] P. Giannozzi *et al.*, J. Phys.: Condens. Matter. **21**, 395502 (2009).
[29] P. Giannozzi *et al.*, J. Phys.: Condens. Matter **29**, 465901 (2017).
[30] P. Giannozzi, O. Baseggio, P. Bonfà, D. Brunato, R. Car, I. Carnimeo, C. Cavazzoni, S. de Gironcoli, P. Delugas, F. Ferrari Ruffino, A. Ferretti, N. Marzari, I. Timrov, A. Urru, and S. Baroni, J. Chem. Phys. **152**, 154105 (2020).
[31] A. Dal Corso, Comput. Mater. Sci. **95**, 337 (2014).
[32] N. Marzari, A. A. Mostofi, J. R. Yates, I. Souza, and D. Vanderbilt, Rev. Mod. Phys. **84**, 1419 (2012).
[33] N. Marzari and D. Vanderbilt, Phys. Rev. B **56**, 12847 (1997).
[34] I. Souza, N. Marzari, and D. Vanderbilt, Phys. Rev. B **65**, 035109 (2001).
[35] A. A. Mostofi, J. R. Yates, Y.-S. Lee, I. Souza, D. Vanderbilt, and N. Marzari, Comput. Phys. Commun. **178**, 685 (2008).
[36] A. A. Mostofi, J. R. Yates, G. Pizzi, Y.-S. Lee, I. Souza, D. Vanderbilt, and N. Marzari, Comput. Phys. Commun. **185**, 2309 (2014).
[37] G. Pizzi *et al.*, J. Phys.: Condens. Matter **32**, 165902 (2020).
[38] M. L. Sancho, J. L. Sancho, J. L. Sancho, and J. Rubio, J. Phys. F **15**, 851 (1985).
[39] Q. Wu, S. Zhang, H.-F. Song, M. Troyer, and A. A. Soluyanov, Comput. Phys. Commun. **224**, 405 (2018).

[40] N. F. Mott and H. Jones, *The Theory of the Properties of Metals and Alloys* (Oxford University Press, Oxford, 1958).
[41] Y. Matsumoto, Y. Haga, N. Tateiwa, H. Aoki, N. Kimura, T. Yamamura, E. Yamamoto, T. D. Matsuda, Z. Fisk, and H. Yamagami, J. Phys. Soc. Jpn. **85**, 104709 (2016).
[42] S. Regmi, M. M. Hosen, B. Ghosh, B. Singh, G. Dhakal, C. Sims, B. Wang, F. Kabir, K. Dimitri, Y. Liu, A. Agarwal, H. Lin, D. Kaczorowski, A. Bansil, and M. Neupane, Phys. Rev. B **102**, 165153 (2020).
[43] M. X. Sprague, S. Regmi, B. Ghosh, A. P. Sakhya, M. I. Mondal, I. Bin Elius, N. Valadez, B. Singh, T. Romanova, D. Kaczorowski, A. Bansil, and M. Neupane, Phys. Rev. B **110**, 045130 (2024).
[44] L. Zhao *et al.*, Phys. Rev. B **83**, 140508(R) (2011).
[45] M. D. Watson, P. Dudin, L. C. Rhodes, D. V. Evtushinsky, H. Iwasawa, S. Aswartham, S. Wurmehl, B. Büchner, M. Hoesch, and T. K. Kim, npj Quantum Mater. **4**, 36 (2019).
[46] C. Tresca and G. Profeta, Phys. Rev. B **95**, 165129 (2017).
[47] A. Ptok, M. Sternik, K. J. Kapcia, and P. Piekarz, Phys. Rev. B **99**, 134103 (2019).
[48] J. Chen, K. Semeniuk, Z. Feng, P. Reiss, P. Brown, Y. Zou, P. W. Logg, G. I. Lampronti, and F. M. Grosche, Phys. Rev. Lett. **116**, 127001 (2016).
[49] M. A. Monge, M. Biasini, G. Ferro, M. Gemmi, G. Satta, S. Massidda, P. Lejay, and A. Continenza, Phys. Rev. B **65**, 035114 (2002).
[50] A. Damascelli, Z. Hussain, and Z.-X. Shen, Rev. Mod. Phys. **75**, 473 (2003).
[51] S. Hüfner, *Photoelectron Spectroscopy: Principles and Applications* (Springer, New York, 2013).
[52] W. Eberhardt and F. J. Himpsel, Phys. Rev. B **21**, 5572 (1980).
[53] S. V. Borisenko, D. V. Evtushinsky, Z.-H. Liu, I. Morozov, R. Kappenberger, S. Wurmehl, B. Büchner, A. N. Yaresko, T. K. Kim, M. Hoesch, T. Wolf, and N. D. Zhigadlo, Nat. Phys. **12**, 311 (2016).
[54] K. Momma and F. Izumi, J. Appl. Crystallogr. **44**, 1272 (2011).
[55] A. Kokalj, Comput. Mater. Sci. **28**, 155 (2003).